polymers

Review

Atomistic Studies of Mechanical Properties of Graphene

Guoxin Cao

Key Laboratory of High Energy Density Physics Simulation (HEDPS),
Center for Applied Physics and Technology, Department of Mechanics and Engineering Science,
College of Engineering, Peking University, Beijing 100871, China; E-Mail: Caogx@pku.edu.cn;
Tel.: +86-010-62756284

Abstract: Recent progress of simulations/modeling at the atomic level has led to a better understanding of the mechanical behaviors of graphene, which include the linear elastic modulus E, the nonlinear elastic modulus D, the Poisson's ratio v, the intrinsic strength σ_{int} and the corresponding strain ε_{int} as well as the ultimate strain ε_{max} (the fracture strain beyond which the graphene lattice will be unstable). Due to the two-dimensional geometric characteristic, the in-plane tensile response and the free-standing indentation response of graphene are the focal points in this review. The studies are based on multiscale levels: including quantum mechanical and classical molecular dynamics simulations, and parallel continuum models. The numerical studies offer useful links between scientific research with engineering application, which may help to fulfill graphene potential applications such as nano sensors, nanotransistors, and other nanodevices.

Keywords: graphene; atomistic simulation; mechanical property

1. Introduction

1.1. Brief Overview of Graphene

Since its discovery in 2004, graphene has attracted extensive research investigations, thanks to its remarkable electrical, thermal, chemical and mechanical properties: (a) high thermal conductivity (5000 W/mK) [1]; (b) high charge carrier mobility at room temperature (15,000 cm^2/Vs) [2]; (c) high specific surface area (2630 m^2/g) [3]; and (d) high elastic modulus (1.02 TPa) and intrinsic strength (130 GPa) [4], which promise wide range of their potential applications in nano devices (e.g., sensors or

resonators), graphene-based composites and so on [5–9]. In general, graphene includes monolayer, bilayer or few layers ($n < 10$) of covalently bonded carbon atoms, and the neighboring layers are separated by the van der Waals (vdW) distance (~0.335 nm).

The mechanical properties of graphene must be fully understood in order to fulfill its promises. Graphene can be considered as a two dimensional (2D) structure due to its nanoscale thickness, and thus, the in-plane tensile behavior is the most important mechanical behavior. Perhaps the most fundamental phenomenological mechanical properties of graphene are the elastic modulus E, the Poisson's ratio v and the intrinsic strength σ_{int}. Several experimental attempts have been employed to measure the elastic modulus of graphene. Currently, free standing indentation testing based on atomic force microscope (AFM) is the most effective way to measure the elastic modulus of graphene: Lee *et al.* [4] reported the value of E of 1.02 TPa of graphene monolayer; Frank *et al.* [10] determined a value of E of 0.5 TPa of a stack of graphene sheets ($n < 5$). Using an instrumented nanoindenter, Zhang and Pan [11] also measured the elastic modulus of monolayer (~0.89 TPa), bilayer (~0.39 TPa) and multiple layer graphene sheets, and they reported that the elastic stiffness of graphene decreases with the increase of the number of layers. A much higher elastic modulus was estimated by Lee *et al.* [12] through measuring the strain applied by a pressure difference across graphene membranes using Raman spectroscopy and the estimated elastic moduli of monolayer and bilayer graphene are 2.4 and 2.0 TPa, respectively. The value of the Poisson's ratio v cannot be directly measured in experiments, which is typically determined from the numerical simulations. With the help of numerical simulations, the intrinsic strength σ_{int} of graphene monolayer is estimated as ~130 GPa from the inverse analysis of the free standing indentation results by Lee *et al.* [6] (the thickness of graphene is assumed as 0.335 nm). In addition, Lindahl *et al.* [13] determined the bending rigidity of the bilayer graphene as ~35.5 eV based on the snap-through behavior of convex buckled graphene membranes under the applied electrostatic pressure.

Since the experiments at nanoscale are highly challenging to perform, theoretical and numerical studies have emerged as an effective way to investigate the intrinsic mechanical properties of graphene. These studies can provide critical insights on the mechanical behavior of graphene.

1.2. Current Status of Theoretical and Numerical Study

The modeling and simulation approaches can be divided into two main categories: (I) atomistic simulations at nanoscale; (II) continuum and structural mechanics modeling. The atomic simulations of graphene are mainly based on the classical molecular dynamics (MD) with empirical interatomic potentials [14–33], the semi-empirical methods (tight-biding) [14,34] and the first-principle quantum mechanics (QM) calculations [35–42].

The QM calculations based on density functional theory (DFT) can explicitly calculate the interactions involving electrons to give the most accurate description of the mechanical behavior but the QM calculation are very computationally expensive and only effective to small system include less than a couple hundred atoms. In order to reduce the computational cost and still explicitly consider the electronic behavior, the semi-empirical (SE) simulations (e.g., tight-binding (TB) method) [43] were developed to solve the molecular orbital functions by replacing complex integrals with simpler empirical parameters and functions. The TB method can be applied to larger systems (including thousands atoms). In order to further increase the size of computational system, the MD simulations are employed, in which the electronic interactions are not explicitly considered and the system potential is only

considered as a function of the lattice coordinates, and thus, the computational cost is significantly reduced and the calculated system can include several million atoms.

With developing the better force field and numerical algorithms (e.g., COMPASS force field [44]), the MD simulations have played a very important role in investigating the mechanical behavior of graphene, including in-plane tension [14–20,45], compression [27], vibration [26] and indentation/free standing indentation [46] as well as out-of-plane bending [29]. Because the elastic modulus of graphene is not sensitive to temperature [15], the molecular mechanics (MM) simulations have been used to study the mechanical behavior of graphene [21–25]. Although the MD/MM approach has a low computational cost in atomic simulation level, there are still the limitations in time scale (less than several ns) and length scale (less than μm) of the models used in MD simulations. Thus, to model the practical application or to compare with the experimental results, it is necessary to develop the continuum model for graphene, which should be able to accurately describe the constitutive behavior obtained from atomistic simulations or experimental testing. The mechanical properties of graphene or CNTs (carbon nanotubes) can be analytically obtained by combining the interatomic potential (e.g., Brenner potential) and continuum theory, which can bypass the MD simulations [33,47,48]. This analytic approach is particularly effective in studying multi-wall CNTs or multiple-layer graphene.

Graphene is typically modeled as a continuum membrane, and the thickness is estimated as ~0.335 nm (the vdW radius of carbon atom). Under small deformation, graphene can be considered to be isotropic, linear elastic material, which is described by the Young's modulus E and the Poisson's ratio v; while under large deformation, graphene shows the strain-soften behavior: the strain-stress relationship is described by two parameters: the second-order linear elastic modulus E and the third-order nonlinear elastic modulus D [4,34]:

$$\sigma = E\varepsilon + D\varepsilon^2 \tag{1}$$

where $D < 0$, so the presence of the second-order term leads to a decrease of stiffness at a larger tensile strain. The intrinsic stress can be determined from the maximum value of σ, which should meet the condition $\partial\sigma/\partial\varepsilon = 0$. The calculated maximum stress (intrinsic strength) and the corresponding strain are:

$$\sigma_{int} = -E^2/4D \text{ at the strain } \varepsilon_{int} = -E/2D \tag{2}$$

Graphene is typically considered as the brittle-like material, and the lattice of graphene is unstable (ruptured) when the strain value is beyond ε_{int}.

1.3. Organization of Review

The review focuses on several recent advances of atomistic studies of the mechanical properties of graphene. At small deformation, the second-order linear elastic constants (C_{ij}, $i, j = 1,2$) of graphene are investigated, based on which the second-order elastic modulus E and the Poisson's ratio v is determined; upon large deformation, the third-order nonlinear elastic constants (C_{iij}, $i, j = 1,2$) are investigated, and the third-order elastic modulus D is determined. In addition, the intrinsic stress σ_{int} and the corresponding strain ε_{int} as well as the ultimate strain ε_{ult} are also discussed. Since the free standing indentation test is the only effective method to measure the mechanical properties of graphene, the free standing indentation response of graphene is also systematically analyzed. Finally, the mechanical response of graphene under free standing indentation is much more complicated than that under in-plane

tension because of the effects of the vdW interaction between indenter tip and graphene, boundary condition and pre-stress. For few-layer graphene, the interlayer interactions also need to be considered.

2. Mechanical Response to In-Plane Tensile Load

Although the tensile test is highly challenging to perform for graphene, the mechanical response to in-plane tension predicted by atomistic simulations can provide us the most fundamental understanding to the mechanical properties of graphene. Based on MM simulations, the initial/deformed structure of graphene is optimized and the total potential energy of system is minimized. MM simulations are carried out using LAMMPS package [49]. The COMPASS forcefield [44] is mainly used to optimize the initial or deformed structures of the free standing graphene monolayer, which is the first ab initio force field that enables an accurate and simultaneous prediction of various condensed phase properties of organic and inorganic materials, and has been widely used in studying carbon-type materials [21–25,50–54]. Reactive empirical bond order (REBO) potential or the adaptive intermolecular reactive empirical bond order (AIREBO) potential is the other type of commonly used forcefield to the mechanical properties of graphene in MM/MD simulations [14,16,17,19,55]. In contrast to the COMPASS forcefield, REBO/AIREBO is able to consider the bond break and reform by setting the C–C bond cut-off length $d_{cut-off}$. Compared with MD simulations, the main concern about MM simulations is that they might not be able to give the correct deformed structure due to the effect of the local minimum potential well (it is more difficult to jump out without the kinetic energy). This is true for the complicated structures, such as protein molecules, but not for the simple structure of the deformed graphene, which can be easily validated using the continuum mechanics theory.

Three basic tensile loading modes, including uniaxial strain/stress and biaxial tension, are applied based on displacement control. The atomic lattice of graphene is six-fold-rotation symmetric, and the in-plane orientation of graphene is typically described by a chirality angle θ: $0° \leq \theta \leq 30°$, where $\theta = 0°$, $30°$ corresponding to the zigzag and armchair directions, respectively. To consider the effect of chirality on the mechanical properties of graphene, the tensile load is applied along the different chirality angles (as shown in Figure 1). To remove the edge effect and simulate the intrinsic properties of graphene, the periodic boundary condition is applied on the in-plane directions (*x*-, *y*-direction) of graphene monolayer and no constraint is applied to the thickness direction (*z*-direction) of graphene. The computational cell includes more than 1000 atoms and the size is about 9 nm × 3 nm which is slightly varying with the chirality angle of graphene. Actually, the simulation results are not dependent on the computational cell size. The strain energy U is a function of the applied tensile strain ε.

2.1. Mechanical Behavior of Monolayer Graphene at Small Deformation

When the tensile strain ε is small (e.g., $\varepsilon < 2\%$), the linear strain-stress relationship is assumed for graphene [4,12,21]. The elastic modulus E and Poisson's ratio v can be directly obtained from the uniaxial stress tension:

$$E = \frac{1}{WL}\frac{\partial^2 U}{\partial \varepsilon^2} \text{ and } v = \frac{\varepsilon_{lat}}{\varepsilon} \tag{3}$$

where W and L are the width and length of the computational cell in MM simulations, respectively, and

ε_{lat} is the lateral strain ($\varepsilon_{lat} < 0$). The value of E can be also calculated based on the uniaxial/biaxial strain tension:

$$C_{11} = \frac{1}{WL}\frac{\partial^2 U}{\partial \varepsilon^2} \text{ (uniaxial) and } C_{11} + C_{12} = \frac{1}{WL}\frac{\partial^2 U}{\partial \varepsilon^2} \text{ (biaxial)} \tag{4}$$

$$E = C_{11}\left(1 - v^2\right) \text{ and } v = -\frac{C_{12}}{C_{11}} \tag{5}$$

where C_{11}, C_{12} are elastic constant. The elastic moduli and Poisson's ratios of graphene determined under tension applied along the different chiralities, obtained from Equations (3)–(5), are shown in Figure 2a,b [21]. To avoid estimating the thickness of graphene t, the 2D modulus (E_t with the unit of N/m) is typically used as the elastic modulus of graphene in most studies. The elastic modulus and Poisson's ratio are determined as $E = 381$–385 N/m and $v = 0.456 \pm 0.008$, respectively. They are close to the upper limit of the reported ranges of the elastic modulus of graphene ($E = 312$–384 N/m) and Poisson's ratio ($v = 0.16$–0.46 [18,21,34,35,47,48,56–58]. It is found that both the values of E and v are actually not sensitive to the chirality angle θ, and thus graphene can be considered to be isotropic under small deformation.

Figure 1. Monolayer graphene under in-plane tension along the different chirality angles: (**a**) Zigzag direction, $\theta = 0°$; (**b**) General direction, $0° < \theta < 30°$; (**c**) Armchair direction, $\theta = 30°$. The periodic boundary condition is applied on both x and y directions.

(a) Zigzag direction, $\theta = 0°$

(b) General direction, $0 < \theta < 30°$

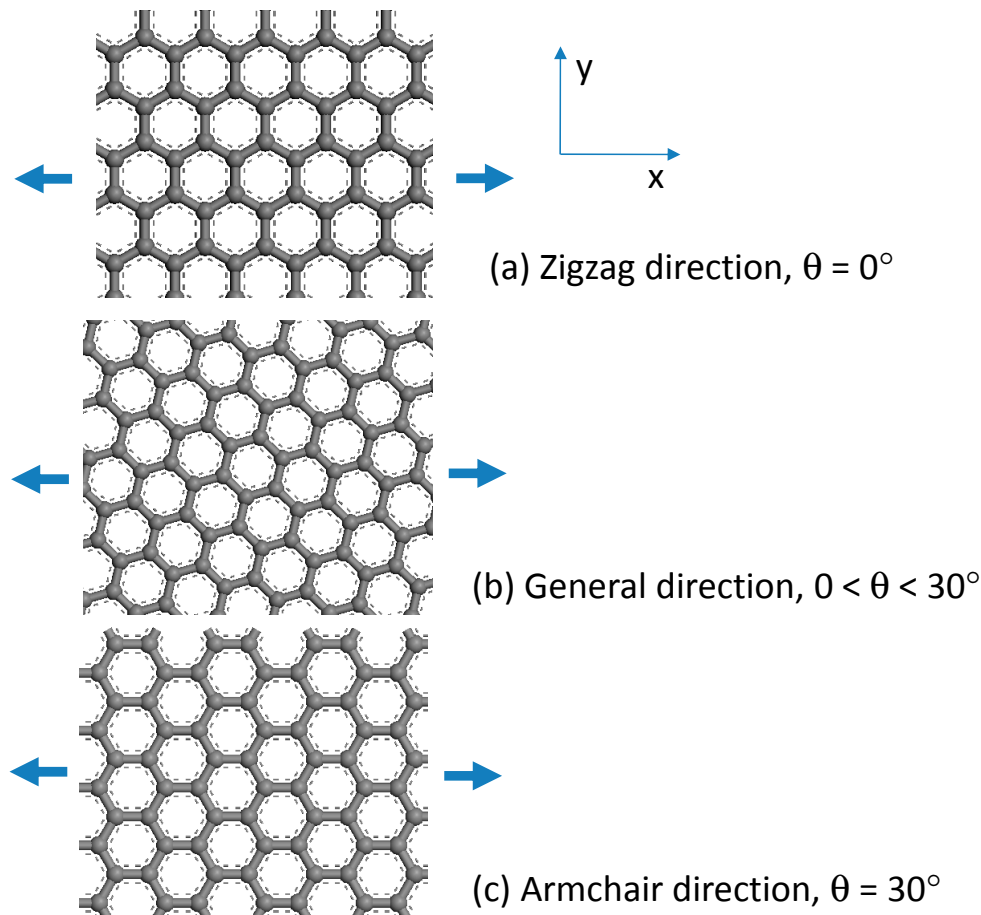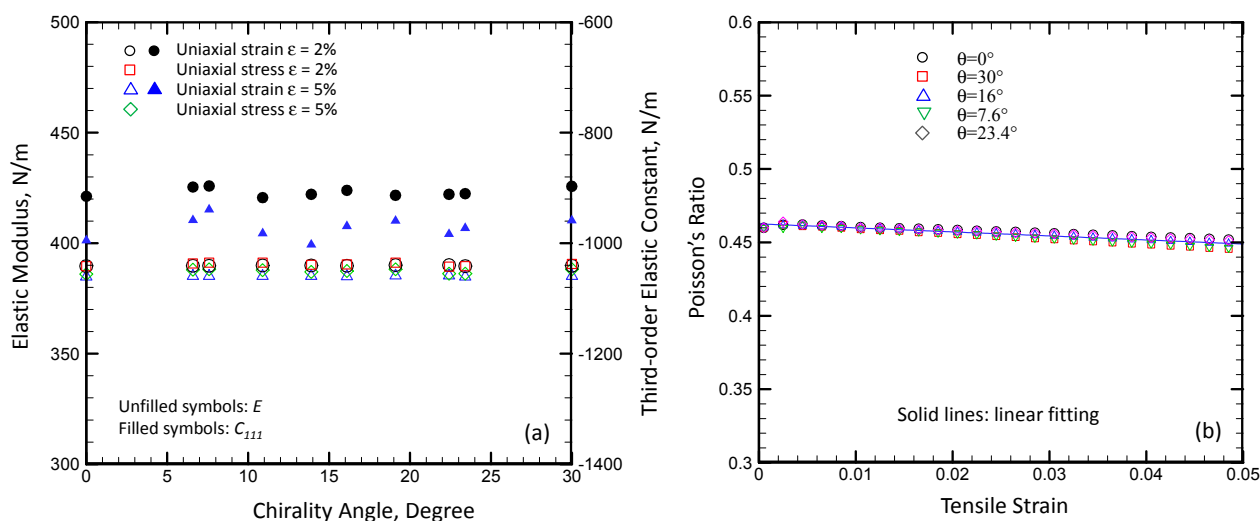(c) Armchair direction, $\theta = 30°$

Figure 2. Elastic properties of monolayer graphene determined from in-plane tension along the different chirality angles: (**a**) the second-order elastic modulus E and the third-order elastic constant C_{111}; and (**b**) Poisson's ratio ν.

The reported values of E and ν of graphene calculated by atomic studies are list in Table 1. The value of E calculated by the REBO/AIREBO potential in MD is slightly lower than that calculated by the COMPASS potential in MM/MD simulations or the DFT simulations. In addition, the value of ν calculated by MM/MD simulations is significantly higher than that calculated by DFT. The reason for the difference is still not clear.

Table 1. Elastic modulus and Poisson's ratio of graphene calculated by atomistic studies.

Reference	Simulation Method	Elastic Modulus (TPa)	Poisson's Ratio
Liu *et al*. [36]	DFT	1.05	0.186
Van Lier *et al* [38]	DFT	1.11	–
Konstantinova [39]	DFT	1.24 ± 0.01	–
Kudin *et al* [40]	DFT	1.029	0.149
Sanchez-Portal [59]	DFT	1.07	0.14–0.19
Hernández [60]	TB	1.206	–
Gupta [61]	MD (Brenner potential)	1.272	0.147
Bao [62]	MD(REBO)	1.026	–
Meo [63]	MM (Morse potential)	0.945	–
Chang [64]	MM (Morse potential)	1.06	0.16
Zhao [14]	MD (AIREBO)	1.01 ± 0.03	0.21 ± 0.01
Zhao [14]	TB	0.91	–
Hajgato [65]	DFT	1.05	–
Hemmasizadeh [66]	MM/CM	0.939	–
Terdalkar [67]	MM (AIREBO)	0.84	–
Zheng [16]	MD (AIREBO)	0.99 ± 0.04	–
Lu [30]	MD (REBO)	0.725	0.398
Shen [68]	MD (modified AIREBO)	1.025	–
Zhang [17]	MD (AIREBO)	0.995	–
Pei [55]	MD (AIREBO)	0.893 (ac)/0.832 (zz)	–
Wei [35]	DFT	1.039	0.169

Table 1. *Cont.*

Reference	Simulation Method	Elastic Modulus (TPa)	Poisson's Ratio
Cadelano [34]	TB	0.931	0.31
Reddy [47]	MM (Tersoff–Brenner)	0.669	0.416
Jiang [69]	MD (COMPASS)	1.0322	–
Neek-Amal [46]	MD, bilayer indentation (Brenner potential)	0.8	–
Neek-Amal [70]	MD indentation (Brenner potential)	0.501 ± 0.032	–
Zhou [21]	MM (COMPASS)	1.167	0.456
Zhou [24]	MM indentation (COMPASS)	1.19	–

2.2. Mechanical Behavior of Monolayer Graphene at Large Deformation

When the tensile strain ε is large (e.g., $\varepsilon > 2\%$), the nonlinear behavior of graphene needs to be considered [21,34,35]. The higher-order terms are need to be introduced into the expression of the strain energy density u (the strain energy per unit area):

$$u = \frac{1}{2!} C_{ij} \varepsilon_i \varepsilon_j + \frac{1}{3!} C_{ijk} \varepsilon_i \varepsilon_j \varepsilon_k + \frac{1}{4!} C_{ijkl} \varepsilon_i \varepsilon_j \varepsilon_k \varepsilon_l + \dots \tag{6}$$

where ε_{ij} is Lagrange strain, and C_{ij}, C_{ijk} and C_{ijkl} are the second-order, third-order and fourth-order elastic constants, respectively. Because of the six-fold-symmetry of graphene, the subscript $i, j, k, l = 1, 2$, representing the zigzag and armchair directions, respectively. For the aforementioned three basic tensile loading modes, the strain energy density is expressed as:

$$u_i = \frac{1}{2!} C_{ii} \varepsilon^2 + \frac{1}{3!} C_{iii} \varepsilon^3 + \dots \quad (i = 1, 2) \text{ (uniaxial strain tension)} \tag{7}$$

$$u = \frac{1}{2} \left(C_{11} + C_{22} + 2C_{12} \right) \varepsilon^2 + \frac{1}{3} \left(2C_{111} - C_{222} + 3C_{112} \right) \varepsilon^3 + \dots \text{ (biaxial tension)} \tag{8}$$

$$u_1 = \frac{1}{2} \left(C_{11} + C_{22} v^2 - 2C_{12} v \right) \varepsilon_1^2 + \frac{1}{6} \left\{ C_{111} \left(1 + 3v^2 \right) - C_{222} \left(v^3 + 3v^2 \right) + 3C_{112} \left(v^2 - v \right) \right\} \varepsilon_1^3 + \dots$$

$$u_2 = \frac{1}{2} \left(C_{22} + C_{11} v^2 - 2C_{12} v \right) \varepsilon_2^2 + \frac{1}{6} \left\{ C_{222} \left(1 + 3v \right) - C_{111} \left(v^3 + 3v \right) + 3C_{112} \left(v^2 - v \right) \right\} \varepsilon_2^3 + \dots \tag{9}$$

(uniaxial stress tension)

Typically, the forth and even higher order terms of strain are neglected in strain energy density expression and the in-plane linear elasticity is considered to be isotropic [21,34–36]. The mechanical properties of graphene monolayer can be described by the second-order linear elastic modulus E and the third-order nonlinear elastic modulus D, and they can be determined as:

$$E = \left. \frac{\partial^2 u}{\partial \varepsilon^2} \right|_{\varepsilon=0} = \left(C_{11}^2 - C_{12}^2 \right) / C_{11} \tag{10}$$

$$D_1 = \frac{1}{2} \left\{ C_{111} \left(1 + 3v^2 \right) - C_{222} \left(v^3 + 3v^2 \right) + 3C_{112} \left(v^2 - v \right) \right\}$$

$$D_2 = \frac{1}{2} \left\{ C_{222} \left(1 + 3v \right) - C_{111} \left(v^3 + 3v \right) + 3C_{112} \left(v^2 - v \right) \right\} \tag{11}$$

If the nonlinear behavior is assumed to be isotropic, the third-order nonlinear elastic modulus $D = (D_1 + D_2)/2$. The values of C_{111}, C_{222} and D are negative for graphene, and thus graphene is a strain-soften material under large deformation. The values of C_{111} for graphene along the different chirality angles [21] are also displayed as filled symbols in Figure 2a. It is found that the values of nonlinear elastic constants are not related to the value of θ either and graphene can be also considered to be isotropic under a large deformation. In addition, the magnitude of the values of C_{111} and C_{222} slightly decrease with the increase in the tensile strain ε.

2.3. Intrinsic Strength of Monolayer Graphene

The elastic modulus E of monolayer graphene is typically measured by free standing indentation technique based on AFM, whereas the intrinsic stress σ_{int} cannot be directly measured, which is determined from the inverse analysis of the experimental data with the help of finite element modeling (FEM) [4,71]. In FEM, the free standing indentation behavior is modeled based on the material model including the measured value of E and the assumed value of D for graphene (with the same geometry as tested in experiments). By matching the breaking indentation force calculated from FEM with its experimental counterpart, the value of D can be identified, and the values of σ_{int} and ε_{int} are then calculated from Equation (2). Based on the aforementioned approach, Lee *et al*. [4] reported $\sigma_{int} = 42 \pm 4$ N/m (the second order Piola-Kirchoff (2nd-PK) stress) and $\varepsilon_{int} = 0.25$ (Lagrange strain). There are two assumptions used in the aforementioned approach: (I) the bending stiffness of graphene is neglected; (II) the difference between the mechanical behavior defined by Equation (1) and its true behavior in free standing indentation is neglected. Actually, the second assumption is not true based on our recent work [72].

The values of σ_{int} and ε_{int} can be also determined from MD simulations based on the REBO potential or AIREBO potential [14,16,17,19,55]. In these potentials, the C–C bond is broken when the deformed bond length is larger than the C–C bond cut-off length $d_{cut-off}$ (e.g., ~0.2 nm), and then the lattice of Graphene is ruptured. σ_{int} and ε_{int} are the maximum values of the simulated strain-stress curve from MD method. Thus, graphene shows the brittle-like behavior: it is failed when the applied tensile strain is larger than ε_{int}. The reported results are $\sigma_{int} = 25.9$–39.5 N/m, $\varepsilon_{int} = 0.14$–0.33, and the zigzag direction has a higher values of σ_{int} and ε_{int} than the armchair direction. It should be noted that the accuracy of the values σ_{int} and ε_{int} determined in MD/MM simulations highly depends on the selected bond cut-off length, which is empirically determined.

DFT simulations are also employed to determine the values of σ_{int} and ε_{int}. Liu *et al*. [36] calculated the phonon spectrum of monolayer graphene under uniaxial stress tension based on DFT, and they suggested that the maximum stress will correspond to the first occurrence of phonon instability, based on which they reported that $\sigma_{int} = 31.1, 30.3$ N/m and $\varepsilon_{int} = 0.3, 0.21$ along zigzag and armchair direction, respectively. Wei *et al*. calculated the uniaxial/biaxial strain tension response of graphene based on DFT [35]. They first determined the value of the second-order, third-order and higher order elastic constants by fitting the strain energy of graphene (obtained by DFT) as the continuum equations, and the strain-stress curve (under uniaxial stress tension) is rebuilt from the obtained elastic constants, based on which the values of σ_{int} and ε_{int} are finally identified ($\sigma_{int} = 31.0, 28.9$ N/m and $\varepsilon_{int} = 0.25, 0.19$ along zigzag and armchair direction, respectively). From the strain-stress curve they built, graphene shows the ductile-like behavior: when the tensile strain is larger than ε_{int}, graphene lattice can still support an

amount of stress (lower than σ_{int}), especially along the zigzag direction. Table 2 shows the reported values of σ_{int} and ε_{int}, which shows a very large varying range.
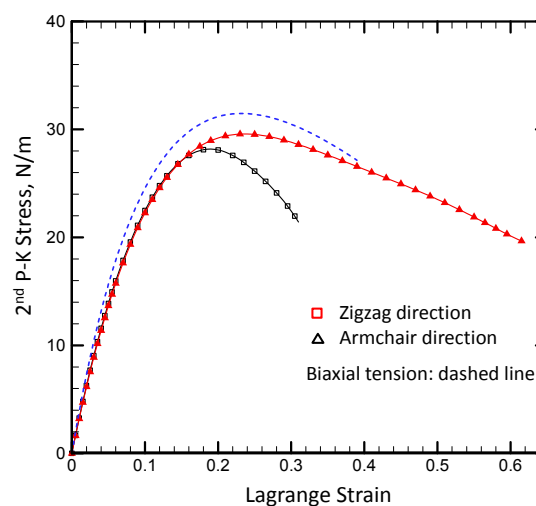
Table 2. The intrinsic strength (the second-order Piola-Kirchhoff stress) and the corresponding Lagrange strain of graphene monolayer.

Reference	Method	Strength (N/m) σ_{int}	Strain ε_{int}
Lee *et al.* [4]	Experiment	42 ± 4	0.25
Liu *et al.* [36]	DFT	31.1 (zz) 30.3 (ac)	0.30 (zz) 0.21 (ac)
Zhao [14]	AIREBO	34.5 (ac) 29.4 (zz)	0.22 (zz) 0.14 (ac)
Marianetti [37]	DFT	25.7	–
Zheng [16]	REBO	35.8 (zz)	0.23 (zz)
Lu [19]	REBO	28.1 (zz) 25.9 (ac)	0.33 (zz) 0.2 (ac)
Zhang [17]	AIREBO	35.2 (zz) 30.6 (ac)	0.21 (zz) 0.14 (ac)
Pei [55]	AIREBO	39.5 (zz) 35.0 (ac)	0.30 (zz) 0.19 (ac)
Wei [35]	DFT	31.0 (zz) 28.9 (ac)	0.25 (zz) 0.19 (ac)
Wei [71]	FEM	30.1	0.23
Cadelano [34]	TB	35.0 (zz) 51.8 (ac)	0.22 (zz) 0.33 (ac)

zz: along zigzag direction; ac: along armchair direction.

The strain-stress relationship of graphene determined directly under uniaxial stress tension by DFT (as shown in Figure 3) clearly show the ultimate strain of graphene (failure strain, ε_{max}) is significantly higher than ε_{int}: along zigzag and armchair directions, $\varepsilon_{int} = 0.23, 0.19$; whereas $\varepsilon_{max} = 0.6, 0.3$ [72]. This also shows the strong anisotropic fracture resistance of graphene: graphene has a much stronger failure strain along zigzag direction than that along armchair direction.

Figure 3. Relationship between the second P-K stress and Lagrange strain of graphene determined under uniaxial/biaxial stress tension.

The different failure strains determined from DFT and MD are mainly caused by the different C–C bond behavior. In DFT simulations, the C–C bond depends on the electrons' behavior explicitly calculated in the simulations, which is a superposition effect of both the electrostatic attraction (between electrons and nucleus) and repulsion (between electrons). Thus, the bond shows a nonlinear behavior

and there is no cut-off feature at the maximum load as defined in MD simulations. In addition, the third-order elastic modulus D calculated from DFT is actually not a constant under a very large deformation ($\varepsilon > 0.05$), which decreases with the value of ε: $D = D' + \lambda\varepsilon$, where the fitting parameters $D' < 0$ and $\lambda > 0$, *i.e.*, the effective modulus E' nonlinearly decreases with ε (as shown in Figure 4), which can be expressed as:

$$E' = \partial\sigma/\partial\varepsilon = E + 2D'\varepsilon + 3\lambda\varepsilon^2 \tag{12}$$

Thus, the values of σ_{int} and ε_{int} calculated from the conventional method (Equation (2)) are not constants and increase with ε, as shown in Figure 5, which might be one of the main reasons why there is a large variation for the reported values of σ_{int} and ε_{int}.

Figure 4. Effective modulus of graphene (E') determined under uniaxial/biaxial tension with different Lagrange strain. The dashed lines are the fitting curves as Equation: $E' = E + 2D'\varepsilon + 3\lambda\varepsilon^2$.
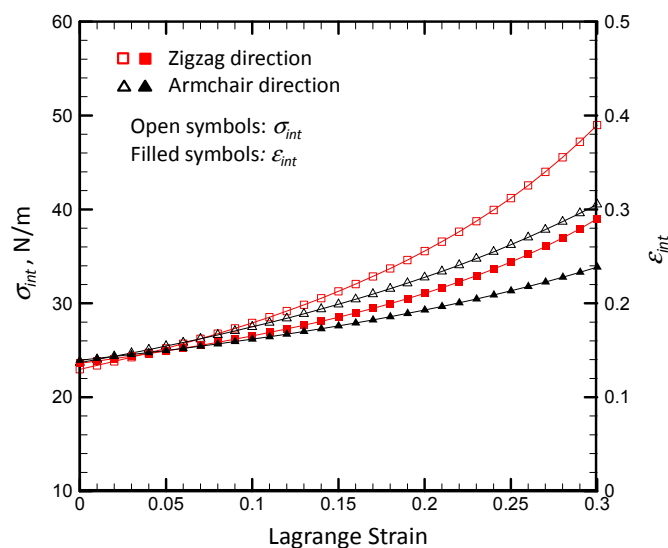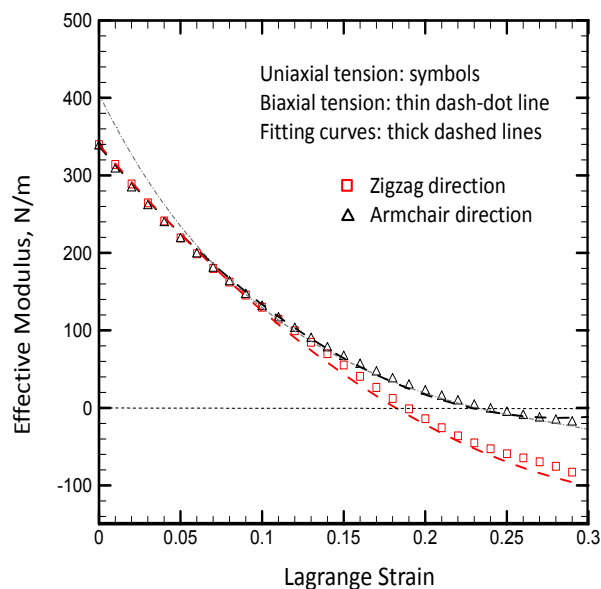

Figure 5. Intrinsic strength σ_{int} and the corresponding strain ε_{int} of monolayer graphene calculated from Equation (2).

3. Mechanical Response to Free Standing Indentation Load

In indentation experiments, graphene is mounted on the SiO_2 substrate with cylindrical holes, and graphene is considered to be strongly bonded with the substrate due to the vdW interaction between graphene and substrate [12,73]. Figure 6a shows the schematic of monolayer graphene under free standing indentation test. In the classic free standing indentation analysis of thin films, the following assumptions are made: (a) the bending stiffness of graphene is approximated as zero; (b) the indenter tip size effect is neglected, *i.e.*, the thin film is loaded by a concentrated force; and (c) the thin film is under the clamped boundary condition. Thus, similar to in-plane tensile load, the response of thin film to free-standing indentation load is the in-plane strain solely. To effectively compare with the mechanical behavior determined from in-plane tensile response of graphene, the indenter tip can be further simplified as cylindrical shape (the axis of cylinder is along y-direction and the cylinder length is equal to the width of graphene sheet), as shown in Figure 6b. In this way, the free standing indentation deformation of thin film with the clamped boundary condition under a cylindrical indenter tip is similar to that in uniaxial strain stretching condition.

Figure 6. (**a**) Schematic of monolayer graphene under free standing indentation test acted by atomic force microscope (AFM); and (**b**) Schematic of the computational model of monolayer graphene under free standing indentation with a cylindrical tip.
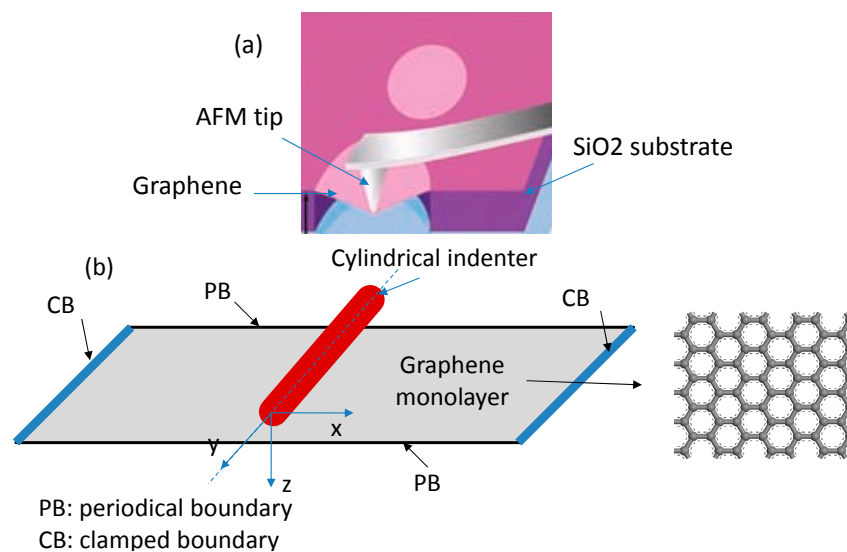
3.1. Mechanical Behavior of Monolayer Graphene to Small Deformation

In free standing indentation, the work done by the indenter tip is equal to the system strain energy U, which is expressed as:

$$U = \int_0^\delta P d\delta \quad \text{or} \quad P = dU / d\delta \tag{13}$$

where P is the indentation force acting on graphene membrane, δ is the deflection of membrane under the indenter tip, which will be considered to be equal to the indenter tip displacement δ_t because δ_t is much easier measured in experiments. According to the geometrical relationship as well as $\delta \approx \delta_t$, the relationship between in-plane strain ε and δ_t will meet the following equation [24]:

$$\varepsilon = \sqrt{4\left(\delta_{\mathrm{t}}/L\right)^2 + 1} - 1 \approx k\left(\delta_{\mathrm{t}}/L\right)^2 \tag{14}$$

where L is the length of monolayer graphene, and the fitting parameter $k = 1.982$ if under the small deformation. According to Equations (4), (5), (13) and (14), the relationship between the indentation force and the indenter tip displacement is derived as following:

$$\frac{P}{W} = \frac{2k^2 E}{1 - v^2}\left(\frac{\delta_{\mathrm{t}}}{L}\right)^3 \tag{15}$$

where W is the width of monolayer graphene. Then, the elastic modulus E of graphene can be fitted from the P-δ_{t} relationship measured in the indentation test. In MM simulations, δ_{t} is the applied displacement of indenter tip and δ is calculated from the vertical deflection of the center of graphene sheet.

The elastic modulus of graphene with the various ratios of graphene length to indenter tip radius (L/R) are shown in Figure 7, displayed as the ratio of $E_{\mathrm{in}}/E_{\mathrm{t}}$, where E_{in} and E_{t} are the elastic modulus determined from free standing indentation and in-plane uniaxial tension, respectively [24]. The value of E_{in} in the figure is obtained by fitting the MM simulation results as Equation (15) and the fitting tensile strain range $\varepsilon \leq 2.5\%$ which matches with the corresponding value used in experiments. In Figure 7, the circles represent changing the value of L while keeping R constant and the squares represent changing the value of R while keeping L constant; while the open and closed symbols represent calculations utilizing δ_{t} and δ, respectively. It is found that the value of E_{in} is significantly larger than E_{t} and the ratio of $E_{\mathrm{in}}/E_{\mathrm{t}}$ gradually decreases with the increase in the value of L/R, but $E_{\mathrm{in}}/E_{\mathrm{t}}$ is still much larger than one even with a very large L/R, e.g., $E_{\mathrm{in}}/E_{\mathrm{t}} \approx 1.2$ with $L/R \approx 50$ (the experimental values: $L/R \approx 30$–90). Thus, the elastic modulus of monolayer graphene will be significantly overestimated in free standing indentation tests. This overestimation is mainly caused by the vdW interaction between the indenter tip and graphene (denoted as the vdW effect) [22].

Figure 7. Elastic modulus of monolayer graphene (E_{in}) with the various ratios of graphene length to indenter tip radius (L/R), displayed as the ratio of $E_{\mathrm{in}}/E_{\mathrm{t}}$. E_{t} is the elastic modulus of monolayer graphene determined from in-plane tension.
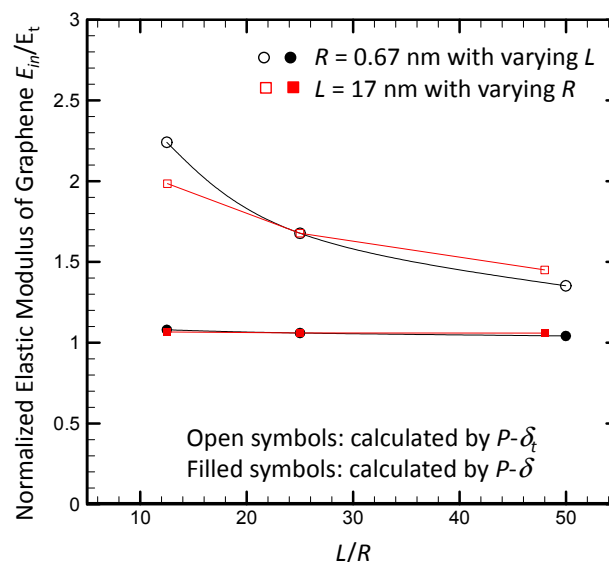
The vdW effect firstly applies the attraction force on graphene when the indenter tip approaching to graphene membrane and the membrane then bulges up to reduce the system potential energy. During this stage, the in-plane strain $\varepsilon > 0$ but the strain energy of system $\Delta U < 0$ (*i.e.*, the indentation force $P < 0$) because $\Delta U = U_g + U_{vdw}$, where the strain energy of graphene (U_g) is positive but with a smaller magnitude than the vdW energy between graphene and indenter tip U_{vdw} (negative) initially. With the tip continually approaching graphene, the magnitude of U_{vdw} will reach the maximum value when the perfect contact between the indenter tip and graphene is realized, and the value of ΔU reaches the minimum (*i.e.*, $P = 0$ and $\delta_t = 0$ because the indentation displacement is counted from $P = 0$). However, the deflection of graphene $\delta > 0$, and thus $\delta > \delta_t$. If based on the conventional assumption: $\delta = \delta_t$, the deflection of grapheme δ is underestimated, and the conventional geometric relationship between δ_t and ε (Equation (14)) cannot be met. Figure 8 shows the relationship between δ_t and ε calculated from MM simulations (displayed as symbols) [24], which is different than the relationship described by Equation (14) (displayed as a solid line). As the reference, the relationship between the true deflection of graphene (δ) and ε is also displayed in the figure, which perfectly matches with Equation (14). Thus, the vdW effect will underestimate the value of δ, which will cause the elastic modulus is overestimated based on Equation (15). In order to further validate this result, plugging the value of δ into Equation (15) instead of δ_t, the value of E_{in} can be recalculated based on the P-δ relationship, also displayed as the ratio of E_{in}/E_t in the Figure 7, which is very close to one even with a very small ratio of L/R [24]. Therefore, if the difference between δ and δ_t caused by the vdW effect is corrected, the elastic modulus of monolayer graphene can be accurately determined from the conventional indentation analysis.

Figure 8. Relationship between indentation displacements (displayed as δ_t/L and δ/L, respectively) and in-plane strain of monolayer graphene under free standing indentation calculated from molecular mechanics (MM) simulations. δ_t and δ are the displacement of indenter tip and graphene, respectively. The solid lines are the fitting curves of Equation (13).
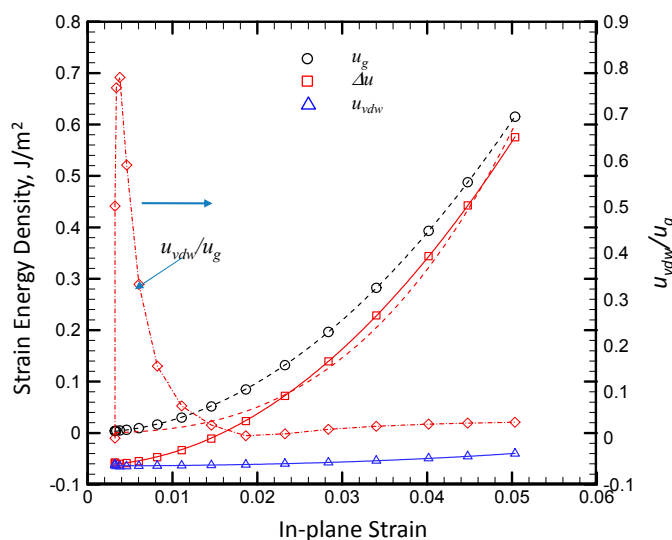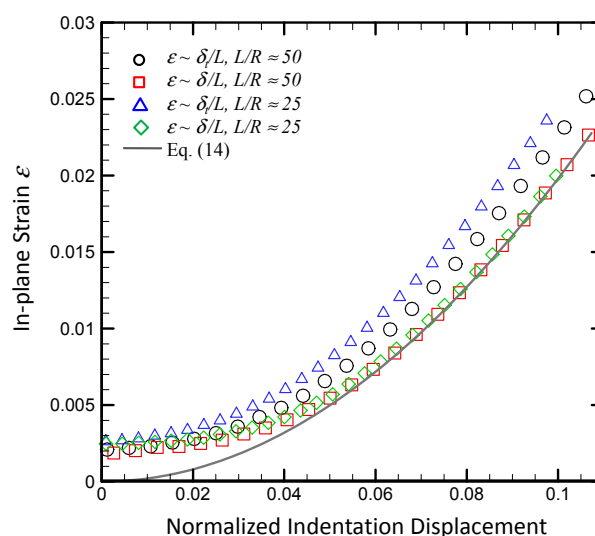

3.2. Mechanical Behavior of Monolayer Graphene to Large Deformation

Monolayer graphene has the nonlinear behavior under large deformation. The nonlinear strain-stress relationship shown by Equation (1) and the strain energy under uniaxial stress tension is expressed by

Equation (7). Under free standing indentation, the system potential energy change (ΔU) includes the strain energy of graphene (U_g) and the vdW interaction energy between indenter tip and graphene (U_{vdw}). In addition, U_g includes both in-plane stretching energy and out-of-plane deformation energy. The MM simulation result of the strain energy density Δu under free standing indentation and its components u_g and u_{vdw}, varying with in-plane strain are shown in Figure 9 [22], where the values of Δu, u_g and u_{vdw} are obtained by their corresponding energy normalized by the area of monolayer graphene. It is found that the value of u_g matches very well with Equation (7), whereas the value of Δu does not follow Equation (7) (displayed as dashed lines), which is caused by u_{vdw} (negative).

Figure 9. MM simulation result of the strain energy density Δu of monolayer graphene under free standing indentation and its components u_g (the strain energy of graphene) and u_{vdw} (the van der Waals (vdW) interaction energy between indenter tip and graphene), varying with in-plane strain. The right side is for the ratio of u_{vdw}/u_g.

The vdW interaction energy density u_{vdw} includes the initial vdW energy density u_0 and the variation of vdW energy density with in-plane strain, which can fitted as [22]:

$$u_{vdw} = u_0 + \Delta u_{vdw} = u_0 + \frac{E_{vdw}}{2(1-v^2)}\varepsilon^2 + \frac{1}{6}c_{vdw}\varepsilon^3 \tag{16}$$

Because u_g matches very well with Equation (7), the value of Δu will be expressed as:

$$\Delta u = u_g + u_{vdw} = u_0 + \frac{1}{2(1-v^2)}\left(E_{vdw} + E_g\right)\varepsilon^2 + \frac{1}{6}\left(c_{vdw} + c_g\right)\varepsilon^3 \tag{17}$$

where $u_g = \dfrac{E_g}{2(1-v^2)}\varepsilon^2 + \dfrac{1}{6}c_g\varepsilon^3$.

The value of Δu calculated by MM simulations can perfectly match with Equation (17), displayed as solid line in Figure 9. Thus, a new parameter u_0 will be added into the strain energy density expression to represent the initial vdW interaction, and both the second- and third- order elastic stiffness of graphene have the contribution from the vdW interaction: $E = E_g + E_{vdw}$ and $C_{111} = C_g + C_{vdw}$. In addition, the vdW effect will rapidly decreases with the increase in in-plane strain of graphene, which can be represented by the ratio of u_{vdw}/u_g.

The second-order elastic modulus of graphene with varying L/R calculated from the indentation response based on MM simulation is shown in Figure 10, displayed as E_{in}/E_t [22]. In the figure, the value of $R = 0.67$ and L increases and the similar result is obtained for a fixed value of L with varying R. From the figure, the second-order elastic modulus calculated from the indentation response is slightly higher than that determined from in-plane tension and the difference decreases with the increase in L/R: $E_{in}/E_t = 1.08–1.14$ with $L/R = 12.5–50$. The difference between E_{in} and E_t is caused by the vdW effect (represented by E/E_g) and the out-of plane deformation of graphene in free standing indentation (represented by E_g/E_s displayed in Figure 10). With the increase in L/R, the ratio of E_g/E_s decreases, and thus it can be neglected at a very large L/R; whereas the vdW effect is only related to R, and it should be considered because the value of R cannot be reduced in the real indentation tests (e.g., $R = 16.5–27.5$ nm and $L = 1–1.5$ μm) [4]. If neglecting the vdW effect, the second-order elastic modulus is directly determined from the conventional indentation analysis which assumes that the free standing indentation response of thin film is similar to the in-plane tension response (as shown by Equation (7)), which will be significantly lower than its counterpart determined from in-plane tension (denoted as E_0 displayed in Figure 10).

Figure 10. Second-order elastic modulus (displayed as E_{in}/E_t) of monolayer graphene with varying L/R determined under free standing indentation by MM simulations. E_0 is the elastic modulus determined by fitting the strain energy density as Equation (7), in which the vdW effect is neglected.
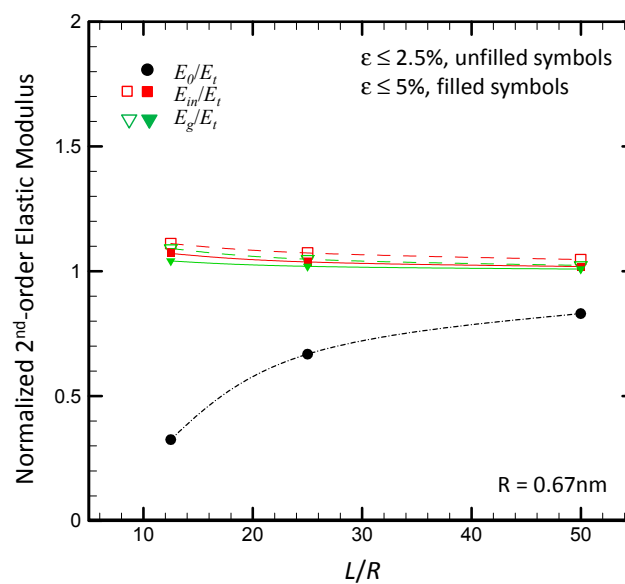
The influence of the vdW effect on the nonlinear term is significantly increased, and there is no effective value of C_{111} is fitted without considering the vdW effect. The third-order elastic constant of graphene with varying L/R calculated from the indentation response based on the MM simulations is shown in Figure 11 [22], displayed as C_{in}/C_t. To show the contributions of the effects of the vdW interaction and out-of-plane deformation to C_{in}, the ratios of C_{in}/C_g and C_g/C_t are also displayed in the figure. Similar to the result of the second-order elastic modulus, the influence of out-of-plane deformation on C_{in} rapidly decreases with the increase of L/R; whereas the vdW effect will be not effectively reduced by increasing L/R. The monolayer graphene deformed in free-standing indentation

has a much higher nonlinear deformation than that in in-plane tension because of the vdW effect which is highly nonlinear. Therefore, if the vdW contribution cannot be accurately described, the third-order elastic modulus cannot be effectively determined. In addition, from Figures 10 and 11, the influence of the vdW effect on both E_{in} and C_{in} decreases with the increase in in-plane strain ε, especially for the value of C_{in}.

Figure 11. Relationship between the third-order elastic constant ratio of graphene (C_{in}/C_t) and the ratio of graphene length to the indenter tip radius, L/R. C_t is the third-order elastic constant determined from in-plane tension.
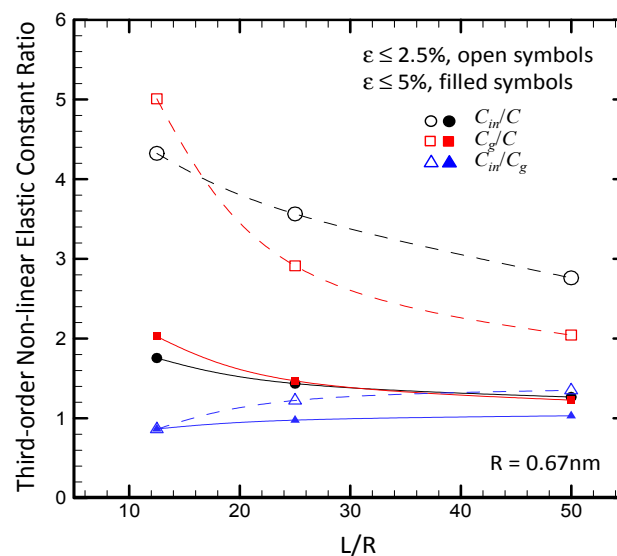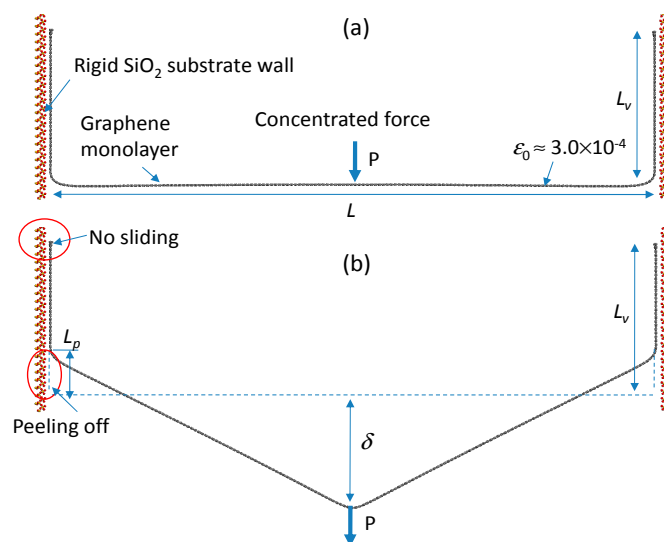

3.3. True Boundary Condition in Free Standing Indentation of Graphene

The clamped boundary condition is typically used in both theoretical/numerical and experimental studies of the free standing indentation response of monolayer graphene, but it is actually not true. In a free standing indentation test, monolayer graphene is mounted on the top surface of SiO$_2$ substrate containing cylindrical holes. It has been observed that graphene membrane does not sever as a rigid lid covering the top of the holes, but a small part of membrane close to the edge of hole bulges into the hole and adhere to the vertical wall of hole [4,12,28,73]. Lee *et al*. [4] suggested that this phenomenon is caused by the vdW interaction between the wall and graphene and they also suggest that the graphene monolayer covered on the substrate is pre-stretched by the vdW interaction. Thus, they added a pre-stress term into the fitting function to fit the measured P-δ_t relationship in indentation tests: $p = a\delta_t + b\delta_t^3$, where the fitting parameters a and b are related to the pre-stress and elastic modulus of graphene, respectively. The pre-tensile stress is estimated to be ranging 0.07–0.74 N/m [4], which is even higher than the fracture strengths of many conventional materials. The pre-strain is determined as about 0.2%–1% by comparing the size of the graphene covered on a substrate hole with the actual hole size, which actually corresponds to the pre-stress of 0.7–3.4 N/m [4]. Thus, there is a significant confliction between the reported pre-stress and pre-strain.

To validate whether or not the vdW interaction between the side wall of substrate and graphene can create a pre-stress in monolayer graphene under free standing indentation, the interaction between SiO$_2$ side wall and graphene is investigated by MM simulations [23]. Figure 12 shows the computational

model to evaluate the interaction strength between the SiO_2 side wall and graphene. In the model, the in-plane strain in the suspend part of graphene created by the vdW attraction between the SiO_2 side wall and graphene is only about 3.0×10^{-4} [23], which is slightly lower than the corresponding value (8.26×10^{-4}) [28] created by the vdW interaction between the carbon sidewall and graphene. These two results match well because the adhesion strength between SiO_2 and graphene (~0.1 J/m^2) [73] is slightly lower than that between carbon and graphene (~0.4 J/m^2) [28]. The pre-strain determined in graphene is not related to the lengths of the suspended part or vertical part of graphene (denoted as L and L_v, respectively). In the reported ranges (L = 10–30 nm and L_v = 5–10 nm), the pre-tensile strain calculated by MM simulations varies very slightly. Therefore, the vdW interaction between the side wall and graphene is not strong enough to create a pre-strain/pre-stress reported by Lee *et al*. [4].

Figure 12. Computational model of graphene with the side wall vdW adhesion in free standing indentation: (**a**) Initial structure; and (**b**) deformed structure under indentation load P.


After applying an indentation load P on the center of the suspended part of graphene, it is not being stretched as it is conventional assumed that graphene in free standing indentation is under a clamped boundary condition; whereas the vertical part of graphene is peeled off from the side wall. During the peeling procedure, there is no sliding observed for the vertical part of grapheme [23]. The vertical part of graphene peeled off from the side wall is converted into the suspended part, and the suspended part is stretched till the vertical part is fully peeled off. Therefore, the vdW interaction between side wall and graphene is also not large enough to maintain a clamped boundary condition of graphene in free standing indentation tests.

Actually, the reported creating mechanism for the phenomenon of a larger size of suspended graphene than the substrate hole size includes several steps [23]: (a) In-plane compression; (b) Buckling; (c) side wall vdW adhesion; and (d) Peeled off, as shown in Figure 13. When graphene is mounted on SiO_2 substrate, the lattice of graphene is compressed because of the lattice mismatch between graphene and SiO_2 as well as the strong adhesion; the compressed graphene is then buckled inside to release the compressive stress acted by the vdW attraction between the substrate side wall and graphene; the released graphene is finally adhere to the side wall by the vdW interaction, which is the graphene structure observed in the experiments. Under the indentation force, the adhered part is firstly peeled off, and then the suspended

part is stretched by the indentation force. Therefore, the true boundary condition of graphene in indentation test will not create a pre-tensile stress/strain but is equivalent to applying a pre-compressive strain. When this pre-compressive strain is fully released, the indentation load begins to stretch the graphene.

Figure 13. Schematic of the creating mechanism of the true boundary condition of graphene in free standing indentation: (**a**) In-plane compression; (**b**) Buckling; (**c**) Adhesion by the vdW interaction between substrate wall and graphene; and (**d**) Peeled off by the indentation load.

(a) In-plane compression

(b) Buckling

(c) VDW adhesion

(d) Peeled off
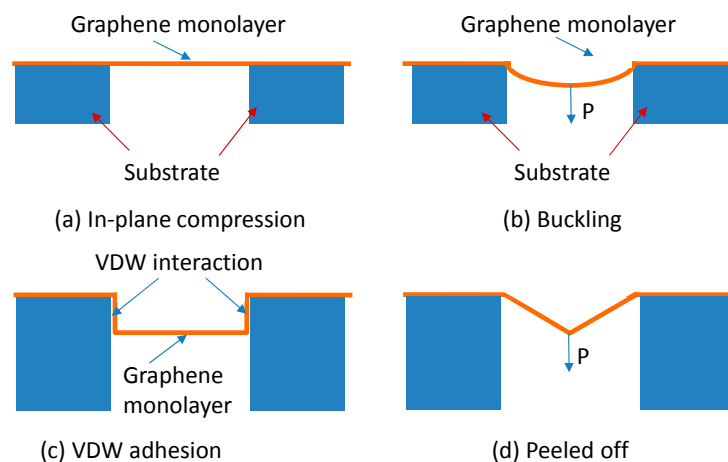
3.4. Pre-Strain Effect on the Indentation Response of Graphene

From the discussion in the above section, it is highly difficult to have a strain free graphene in indentation tests, and thus it is very necessary to investigate the pre-strain effect on the indentation response of graphene. With a pre-strain ε_0, the relationship between in-plane strain ε and the deflection of grapheme δ (Equation (14)) will be rewritten as [23]:

$$\varepsilon = \sqrt{4\left(\delta/L\right)^2 + \left(1+\varepsilon_0\right)^2} - 1 \approx k\left(\delta/L\right)^2 + \varepsilon_0 \tag{18}$$

where $k = 1.963-1.9\varepsilon_0$ with $\varepsilon \leq 5\%$ and $-1\% \leq \varepsilon_0 \leq 1\%$. Thus, if based on the assumption $\delta = \delta_t$, the relationship between indentation force P and indentation displacement δ_t of graphene with a pre-strain ε_0 under a cylindrical indenter tip can be expressed as [23]:

$$\frac{P}{W} = \frac{2k^2 E_{in}}{1-v^2}\left(\frac{\delta_t}{L}\right)^3 + \frac{2kE_{in}\varepsilon_0}{1-v^2}\left(\frac{\delta_t}{L}\right) \tag{19}$$

Noted that with $\varepsilon_0 \leq 0$, the pre-compression will be release by the deflection of graphene (*i.e.*, there is no pre-compressive stress). On the other word, a pre-compressive strain is equivalent to an initial deflection of the suspended graphene ($\delta_0 = L\sqrt{\varepsilon_0/k}$), as shown in Figure 13d, and the effective value of P is measured only when $\delta_t \geq \delta_0$.

The calculated P-δ_t relationship of graphene monolayer by MM simulations is shown in Figure 14, and the values of E_{in} and ε_0 can be determined by fitting the MM results as Equation (19) (the fitting curves are displayed as the solid lines in Figure 14) [23]. Figure 15 show the calculated values of E_{in} (displayed as the ratio of E_{in}/E_t) and ε_0 [23]. With $\varepsilon_0 \leq 0$, MM results do not match very well with Equation (19), and both the values of E_{in} and ε_0 cannot be accurately determined: the value of E_{in} will be

overestimated up to 30% and the error in ε_0 is even larger. However, with $\varepsilon_0 > 0$, there is a good agreement between the MM results and Equation (19), and the determined values of E_{in} and ε_0 match very well with their true values. This difference is mainly caused by the coupling effect between the vdW effect and the pre-strain in graphene. When the value of ε_0 varies from positive to negative, the contact area between the indenter tip and graphene is significantly increased, and thus the vdW effect also increases. As we have discussed, a larger vdW effect will cause a larger difference between δ and δ_t, and thus a higher error in the values of E_{in} and ε_0 will be created base on Equation (19). This will be further validated based on the P-δ relationship of the graphene with the pre-strain. After substituting δ_t with δ in Equation (19), the MM simulation results of the P-δ relationship can match very well with Equation (19), and the values of E_{in} and ε_0 determined from the fitting procedure match very well with their true values (as shown in Figure 15).

> **Figure 14.** The P-δ_t relationship of monolayer graphene determined from free standing indentation. P is the indentation load; δ_t is the indenter tip displacement, normalized by the graphene length L.
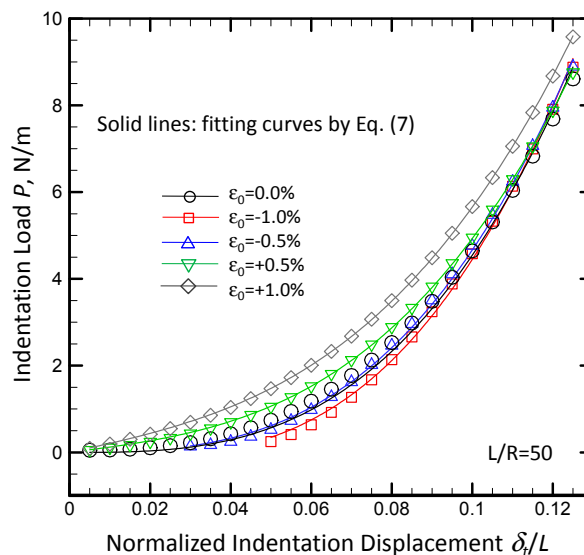

When the difference between δ_t and δ is large, the assumption of $\delta_t = \delta$ used in the classic analysis can actually create a "*fake*" pre-strain ε_0 for the membrane without pre-strain ($\varepsilon_0 = 0$) based on the P-δ_t relationship of graphene shown by Equation (19). The accompanying "*fake*" pre-stress is expressed as:

$$\sigma'_0 = \frac{E_{in}}{1-v^2} \frac{k\left(\delta^3 - \delta_t^3\right)}{\delta_t L^2} \tag{20}$$

where the value of δ is typically larger than δ_t. Thus, there will be a "*fake tensile stress*" in graphene in free standing indentation, which does not show the true pre-stress state of graphene. This can be further validated by the results shown in Figure 15: for the cases with $\varepsilon_0 < 0$, the absolute value of the fitted ε_0 is much lower than its true value. Therefore, the classic indentation analysis (*i.e.*, the P-δ_t relationship) is not able to give the true pre-stain state of graphene. This result also suggests that the pre-tensile stress determined from free indentation tests by Lee *et al.* [4] is overestimated. The corrected value should be determined from the P-δ relationship instead of using the P-δ_t relationship.

Figure 15. The calculated values of the second-order elastic modulus E_{in} and the pre-strain ε_0 of graphene under free standing indentation, displayed as the ratio of E_{in}/E_t.
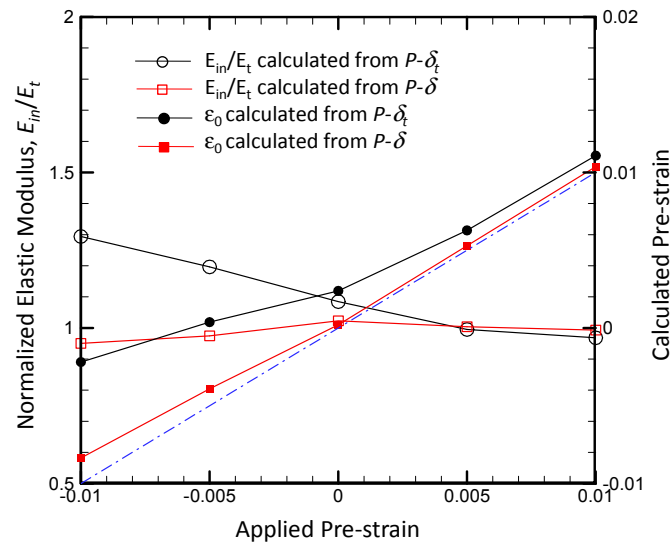
3.5. Indentation Response of Few-Layer Graphene

The indentation response of few-layer graphene (FLG) is more complicated than that of monolayer graphene, which is not only dependent on the mechanical properties of graphene layers but also related to the vdW interactions between graphene layers (denoted as interlayer reactions). It has been discussed in the above sections that the difference between δ_t and δ is increased because of the vdW interaction between indenter tip and graphene (denoted as the vdW effect). For FLG, the vdW effect decreases with the increase in the number of graphene layers in FLG because of the interlayer interactions. However, there is still a large difference between δ_t and δ of FLG [25]. Similar to monolayer graphene, the δ_t-ε relationship does not match with Equation (14) but the δ-ε relationship can match very well if replacing δ_t by δ for FLG with the number of layer n = 1–4. Thus, the P-δ_t curve does not match with Equation (15), whereas the P-δ curve can match well with the Equation after replacing δ_t by δ (as shown in Figure 16). Under a small, the elastic modulus of FLG (E_{FLG}) can be obtained by fitting the P-δ_t curve as Equation (15), deformation displayed in Figure 17, which is normalized by the number of layers n and E_t (the elastic modulus of monolayer graphene determined from in-plane tension). The ratio of E_{FLG}/n of bilayer graphene is slight lower than that of monolayer or four-layer graphene. The lower elastic modulus of bilayer graphene than that of monolayer has been also reported by Neek and Peeters [46] and Lee *et al.* [12]. If based on the P-δ curve, the more accurate modulus of FLG (denoted as E'_{FLG}) can be obtained, displayed as the ratio of E'_{FLG}/nE_t in Figure 17. The value of E'_{FLG}/n slightly increases with n, which is caused by the interlayer reactions.

Figure 16. The relationship between the normalized indentation load *(P/n)* and the normalized indentation displacement $((\delta_t/L)^3$ or $(\delta/L)^3$ of few-layer graphene (FLG) with $n = 1$–4.
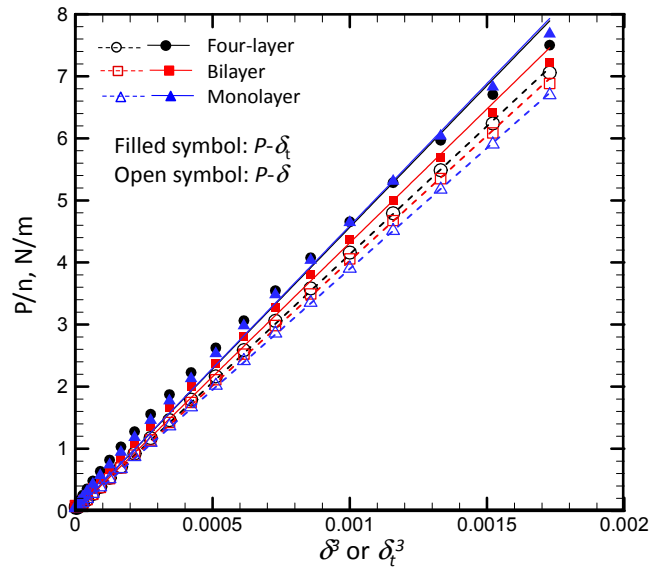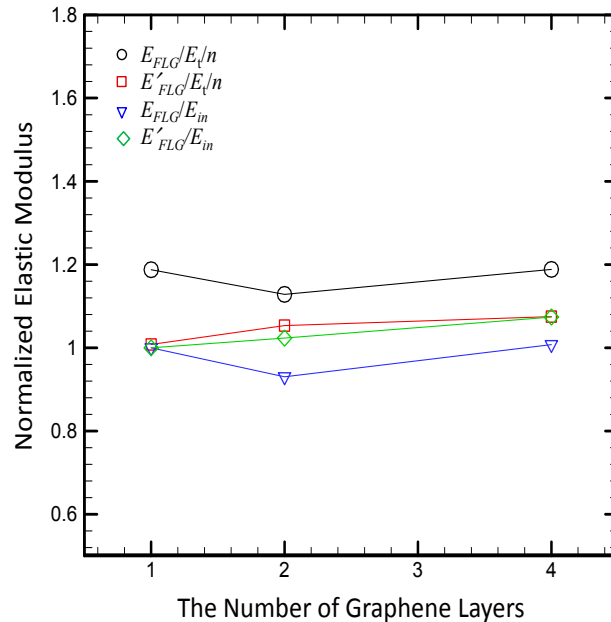

Figure 17. The normalized elastic moduli of FLG determined under small deformation. E_{FLG} and E'_{FLG} are the elastic moduli of FLG determined from free-standing indentation using the δ_t/L-ε relationship and the δ/L-ε relationship, respectively.

For FLG, the contribution from the interlayer interactions should be added into the expression of the strain energy density, and the strain energy density is expressed as:

$$u = \sum_{j=1}^{n} u_{gj} + \sum_{j=1,k=j+1}^{n-1} u_{jk} + u_{\mathrm{vdw}} \qquad (21)$$

where u_{gj} is the strain energy density of the *j*th layer graphene, and u_{jk} represents the interlayer interaction energy density between the *j*th layer and the *k*th layer in FLG, which is also expressed as an

similar function as u_g. Thus, the overall elastic modulus of FLG, $E_{FLG} = E_g + E_i + E_{vdw}$ and the overall nonlinear elastic constant, $C_{FLG} = C_g + C_i + C_{vdw}$, where all components are the linear combination of all layers: $E_g = \sum E_{gj}$, $E_i = \sum E_{jk}$, $C_g = \sum C_{gj}$ and $C_i = \sum C_{jk}$, and the subscripts g and i represent the contributions from graphene layers and the interlayer reactions, respectively. With a large deformation, a higher order term of strain is introduced, and thus the overall strain energy density of FLG is:

$$u = u_0 + \frac{\varepsilon^2}{2(1-v^2)}\left[E_g + E_i + E_{vdw}\right] + \frac{1}{6}\left(C_g + C_i + C_{vdw}\right)\varepsilon^3 \tag{22}$$

By fitting the u-ε relationship calculated from MM simulations as Equation (22), the elastic properties of FLG can be determined. Figure 18 shows the values of E_{gj} and E_{jk} of each layer in FLG ($n = 2$–4), normalized by the value of E_g of monolayer graphene. The values of E_{gj} and E_{jk} are quite close to each other for the different layers in FLG. With the increase of load range ε, the value of E_{gj} is essentially a constant, but E_{jk} significantly decreases. Because E_{jk} is highly nonlinear, it will strongly affect the nonlinear behavior of FLG. The third-order nonlinear elastic constant C_{FLG} is displayed in Figure 19, displayed as a ratio of $C_{FLG}/C_t/n$. The ratio of C_{FLG}/n is significantly higher than that of monolayer of graphene and very close to $(C_g + C_i)/n$, which suggest that the interlayer interaction will strongly affect the nonlinear behavior of FLG and the vdW effect is very weak in FLG. As a reference, the ratio of C'_{FLG}/n of FLG determined from in-plane tension is also displayed in the figure, which is essentially not sensitive to n, and thus, the interlayer interactions will not affect the nonlinear behavior of FLG in-plane tension. In addition, with the increase in loading range, the nonlinear behavior is significantly decreased. Thus, in free standing indentation test, a larger indentation load will give a more accurate result.

Figure 18. The normalized second-order elastic modulus of each graphene layer ($E_{gj}/E_g(1)$ corresponds to integer layer number) and interlayer interaction strength ($E_{jk}/E_g(1)$ refers to the points at fractional layer number) in FLG, where $E_g(1)$ is the value of E_g of the graphene monolayer ($n = 1$).
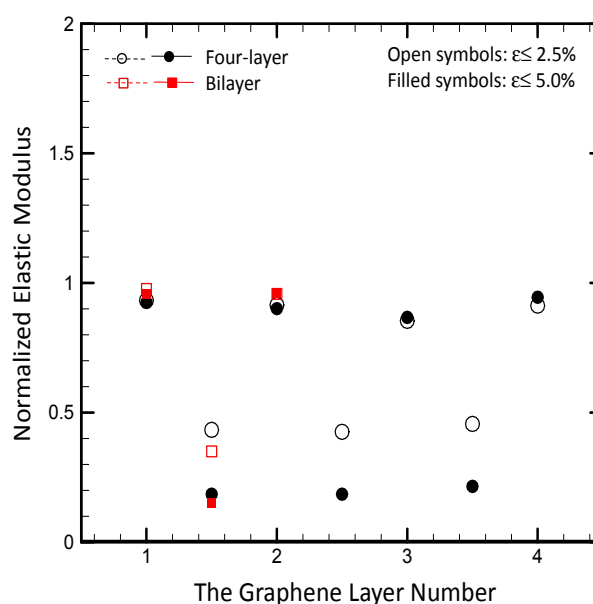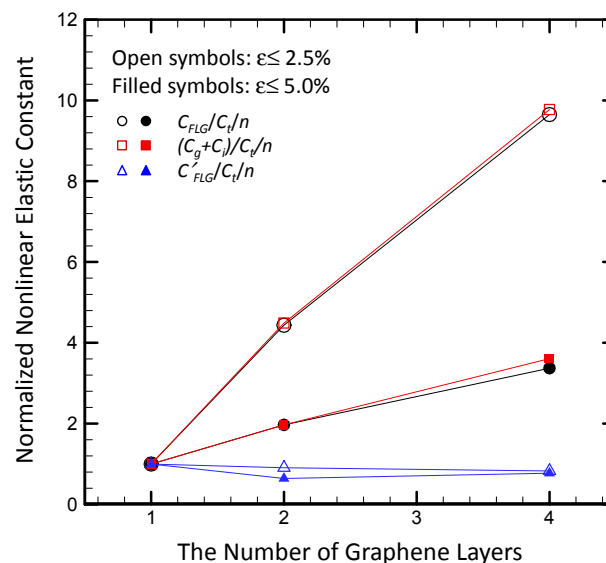
Figure 19. The variation of the normalized third-order nonlinear elastic constant of FLG ($C_{in}/C_t/n$) with the number of layers in FLG. C_t is the third-order nonlinear elastic constant of monolayer graphene determined from in-plane tension.

4. Other Effects on the Mechanical Properties of Graphene

All of the above investigations are based on perfect graphene atomic structures, but it has been reported that the mechanical properties of 2D structures can be heavily affected by structural irregularities, such as defects, dislocations and grain boundaries (GBs). Based on the present manufacturing technology, the presence of irregularities in graphene structure is inevitable, particularly for GBs, because the polycrystalline graphene is the typical product of large-area chemical-vapor-deposition (CVD) synthesis. The effect of GB on the mechanical properties of polycrystalline graphene has attracted wide research interests [74–84]. Lee *et al* found that polycrystalline graphene sheets with grain sizes of 1−5 μm have an elastic modulus of about 965 GPa and an intrinsic strength of about 100 GPa [83], which are lower than their counterparts of pristine graphene (~1 TPa and ~130 GPa).

The crystalline orientations of graphene are different between two domains connected by GBs. At the atomic level, GBs of graphene are typically considered to be formed by the pentagon-heptagon defect which is the commonest topological defect of graphene. Actually, GBs of graphene composed of periodically distributed pentagon-heptagon pairs [78,80,82,84]. The misorientation angle θ of two connected crystalline domain is defined as [82]:

$$\theta = 2\arcsin\frac{b}{2L_d} \tag{23}$$

where *b* is the Burgers vector of dislocations and L_d is the distance between the pentagon-heptagon pair. The low angle GB corresponds to the low-density, large period dislocation structure, while the high angle GB corresponds to the high-density, small-period dislocation structure. The atomic studies also show that the presence of grain boundary will decrease the intrinsic strength of graphene. The strength of GB is highly sensitive to the angle θ and also depends on the loading direction of graphene as well as the arrangement of pentagon-heptagon pairs. For the tension along zigzag direction, the failure strength and

the corresponding strain monotonically increases with the angle θ, while the trend is broken for the tension along armchair direction (with non-monotonic character) [80]. The main reason might be that the normal stress of the C–C bond created by dislocation structure is higher for the low angle GB but lower for the high angle GB.

5. Conclusions

The atomic studies of the mechanical response of graphene under in-plane tension and free standing indentation are briefly reviewed in this paper, which provide a critical link between the science underpinning graphene and its engineering applications. The linear elastic properties (e.g., elastic modulus and Poisson's ratio) under small deformation and the nonlinear elastic properties (e.g., the intrinsic strength) under large deformation are focused in this review. Specifically, the effects of the vdW interaction between indenter tip and graphene, the true boundary condition of graphene in free standing indentation and the pre-strain on the properties of graphene are discussed.

For 2D material or structure, such as graphene, the mechanical properties highly depend on its atomic feature, including its atomic-level thickness, the vdW interaction with indenter tip, substrate or among graphene layers, and geometric singularities (defects). The effects of those factors on the mechanical response are different under the different loading/deformation modes. In the conventional continuum theory, the mechanical properties measured will be different, or even with a very large fluctuation, since the aforementioned factors cannot be properly considered. Therefore, numerical simulations at the atomistic scale can play an important role for understanding the mechanical properties of 2D structures (e.g., grpahene) as well as fulfilling their promises based on its mechanical behavior.

The nanomechanics principles discussed above can be readily extended to other nanoscale materials and structures. It is conceivable that the unique structures and properties of graphene and other nanomaterials will bring a profound impact to the technology, where the atomistic simulation plays a critical role.

Conflicts of Interest

The authors declare no conflict of interest.

References

1. Balandin, A.A.; Ghosh, S.; Bao, W.Z.; Calizo, I.; Teweldebrhan, D.; Miao, F.; Lau, C.N. Superior thermal conductivity of single-layer graphene. *Nano Lett.* **2008**, *8*, 902–907.
2. Bolotin, K.I.; Sikes, K.J.; Jiang, Z.; Klima, M.; Fudenberg, G.; Hone, J.; Kim, P.; Stormer, H.L. Ultrahigh electron mobility in suspended graphene. *Solid State Commun.* **2008**, *146*, 351–355.

3. Steurer, P.; Wissert, R.; Thomann, R.; Mulhaupt, R. Functionalized graphenes and thermoplastic nanocomposites based upon expanded graphite oxide. *Macromol. Rapid Commun.* **2009**, *30*, 316–327.

4. Lee, C.; Wei, X.D.; Kysar, J.W.; Hone, J. Measurement of the elastic properties and intrinsic strength of monolayer graphene. *Science* **2008**, *321*, 385–388.

5. Geim, A.K. Graphene: Status and prospects. *Science* **2009**, *324*, 1530–1534.

6. Novoselov, K.S.; Geim, A.K.; Morozov, S.V.; Jiang, D.; Katsnelson, M.I.; Grigorieva, I.V.; Dubonos, S.V.; Firsov, A.A. Two-dimensional gas of massless dirac fermions in graphene. *Nature* **2005**, *438*, 197–200.

7. Stankovich, S.; Dikin, D.A.; Dommett, G.H.B.; Kohlhaas, K.M.; Zimney, E.J.; Stach, E.A.; Piner, R.D.; Nguyen, S.T.; Ruoff, R.S. Graphene-based composite materials. *Nature* **2006**, *442*, 282–286.

8. Eda, G.; Fanchini, G.; Chhowalla, M. Large-area ultrathin films of reduced graphene oxide as a transparent and flexible electronic material. *Nat. Nanotechnol.* **2008**, *3*, 270–274.

9. Soldano, C.; Mahmood, A.; Dujardin, E. Production, properties and potential of graphene. *Carbon* **2010**, *48*, 2127–2150.

10. Frank, I.W.; Tanenbaum, D.M.; van der Zande, A.M.; McEuen, P.L. Mechanical properties of suspended graphene sheets. *J. Vac. Sci. Technol. B* **2007**, *25*, 2558–2561.

11. Zhang, Y.P.; Pan, C.X. Measurements of mechanical properties and number of layers of graphene from nano-indentation. *Diam. Relat. Mater.* **2012**, *24*, 1–5.

12. Lee, J.U.; Yoon, D.; Cheong, H. Estimation of young's modulus of graphene by raman spectroscopy. *Nano Lett.* **2012**, *12*, 4444–4448.

13. Lindahl, N.; Midtvedt, D.; Svensson, J.; Nerushev, O.A.; Lindvall, N.; Isacsson, A.; Campbell, E.E.B. Determination of the bending rigidity of graphene via electrostatic actuation of buckled membranes. *Nano Lett.* **2012**, *12*, 3526–3531.

14. Zhao, H.; Min, K.; Aluru, N.R. Size and chirality dependent elastic properties of graphene nanoribbons under uniaxial tension. *Nano Lett.* **2009**, *9*, 3012–3015.

15. Zhao, H.; Aluru, N.R. Temperature and strain-rate dependent fracture strength of graphene. *J. Appl. Phys.* **2010**, *108*, doi: 10.1063/1.3488620.

16. Zheng, Y.P.; Wei, N.; Fan, Z.Y.; Xu, L.Q.; Huang, Z.G. Mechanical properties of grafold: A demonstration of strengthened graphene. *Nanotechnology* **2011**, *22*, doi:10.1088/0957-4484/22/40/405701.

17. Zhang, Y.Y.; Pei, Q.X.; Wang, C.M. Mechanical properties of graphynes under tension: A molecular dynamics study. *Appl. Phys. Lett.* **2012**, *101*, doi:10.1063/1.4747719.

18. Wang, L.; Zhang, Q. Elastic behavior of bilayer graphene under in-plane loadings. *Curr. Appl. Phys.* **2012**, *12*, 1173–1177.

19. Lu, Q.; Gao, W.; Huang, R. Atomistic simulation and continuum modeling of graphene nanoribbons under uniaxial tension. *Model. Simul. Mater. Sci. Eng.* **2011**, *19*, doi:10.1088/0965-0393/19/5/054006.

20. Sakhaee-Pour, A. Elastic properties of single-layered graphene sheet. *Solid State Commun.* **2009**, *149*, 91–95.

21. Zhou, L.X.; Wang, Y.G.; Cao, G.X. Elastic properties of monolayer graphene with different chiralities. *J. Phys. Condens. Mater.* **2013**, *25*, doi: 10.1088/0953-8984/25/12/125302.

22. Zhou, L.X.; Wang, Y.G.; Cao, G.X. Van der waals effect on the nanoindentation response of free standing monolayer graphene. *Carbon* **2013**, *57*, 357–362.

23. Zhou, L.X.; Wang, Y.G.; Cao, G.X. Boundary condition and pre-strain effects on the free standing indentation response of graphene monolayer. *J. Phys. Condens. Mater.* **2013**, *25*, doi:10.1088/0953-8984/25/47/475303.

24. Zhou, L.X.; Xue, J.M.; Wang, Y.G.; Cao, G.X. Molecular mechanics simulations of the deformation mechanism of graphene monolayer under free standing indentation. *Carbon* **2013**, *63*, 117–124.

25. Zhou, L.X.; Wang, Y.G.; Cao, G.X. Estimating the elastic properties of few-layer graphene from the free-standing indentation response. *J. Phys. Condens. Mater.* **2013**, *25*, doi:10.1088/0953-8984/25/47/475301.

26. Sakhaee-Pour, A.; Ahmadian, M.T.; Naghdabadi, R. Vibrational analysis of single-layered graphene sheets. *Nanotechnology* **2008**, *19*, doi:10.1088/0957-4484/19/8/085702.

27. Sakhaee-Pour, A. Elastic buckling of single-layered graphene sheet. *Comput. Mater. Sci.* **2009**, *45*, 266–270.

28. Lu, Z.X.; Dunn, M.L. Van der waals adhesion of graphene membranes. *J. Appl. Phys.* **2010**, *107*, doi:10.1063/1.3270425.

29. Wang, Q. Simulations of the bending rigidity of graphene. *Phys. Lett. A* **2010**, *374*, 1180–1183.

30. Lu, Q.; Huang, R. Nonlinear mechanics of single-atomic-layer graphene sheets. *Int. J. Appl. Mech.* **2009**, *1*, 443–467.

31. Neek-Amal, M.; Peeters, F.M. Graphene nanoribbons subjected to axial stress. *Phys. Rev. B* **2010**, *82*, doi:10.1103/PhysRevB.82.085432.

32. Min, K.; Aluru, N.R. Mechanical properties of graphene under shear deformation. *Appl. Phys. Lett.* **2011**, *98*, doi:10.1063/1.3534787.

33. Rajendran, S.; Reddy, C.D. Determination of elastic properties of graphene and carbon-nanotubes using brenner potential: The maximum attainable numerical precision. *J. Comput. Theor. Nanosci.* **2006**, *3*, 382–390.

34. Cadelano, E.; Palla, P.L.; Giordano, S.; Colombo, L. Nonlinear elasticity of monolayer graphene. *Phys. Rev. Lett.* **2009**, *102*, doi:10.1103/PhysRevLett.102.235502.

35. Wei, X.D.; Fragneaud, B.; Marianetti, C.A.; Kysar, J.W. Nonlinear elastic behavior of graphene: *Ab initio* calculations to continuum description. *Phys. Rev. B* **2009**, *80*, doi:10.1103/PhysRevB.80.205407.

36. Liu, F.; Ming, P.M.; Li, J. *Ab initio* calculation of ideal strength and phonon instability of graphene under tension. *Phys. Rev. B* **2007**, *76*, doi:10.1103/PhysRevB.76.064120.

37. Marianetti, C.A.; Yevick, H.G. Failure mechanisms of graphene under tension. *Phys. Rev. Lett.* **2010**, *105*, doi:10.1103/PhysRevLett.105.245502.

38. Van Lier, G.; van Alsenoy, C.; van Doren, V.; Geerlings, P. *Ab initio* study of the elastic properties of single-walled carbon nanotubes and graphene. *Chem. Phys. Lett.* **2000**, *326*, 181–185.

39. Konstantinova, E.; Dantas, S.O.; Barone, P.M.V.B. Electronic and elastic properties of two-dimensional carbon planes. *Phys. Rev. B* **2006**, *74*, doi:10.1103/PhysRevB.74.035417.

40. Kudin, K.N.; Scuseria, G.E.; Yakobson, B.I. C2F, BN, and C nanoshell elasticity from *ab initio* computations. *Phys. Rev. B* **2001**, *64*, doi:10.1103/PhysRevB.64.235406.

41. Wei, Y.J.; Wang, B.L.; Wu, J.T.; Yang, R.G.; Dunn, M.L. Bending rigidity and gaussian bending stiffness of single-layered graphene. *Nano Lett.* **2013**, *13*, 26–30.

42. Faccio, R.; Denis, P.A.; Pardo, H.; Goyenola, C.; Mombru, A.W. Mechanical properties of graphene nanoribbons. *J. Phys.Condens. Mater.* **2009**, *21*, doi:10.1088/0953-8984/21/28/285304.

43. Porezag, D.; Frauenheim, T.; Kohler, T.; Seifert, G.; Kaschner, R. Construction of tight-binding-like potentials on the basis of density-functional theory-application to carbon. *Phys. Rev. B.* **1995**, *51*, 12947–12957.

44. Sun, H. Compass: An *ab initio* force-field optimized for condensed-phase applications—Overview with details on alkane and benzene compounds. *J. Phys. Chem. B.* **1998**, *102*, 7338–7364.

45. Zhu, J.; He, M.; Qiu, F. Effect of vacancy defects on the young's modulus and fracture strength of graphene: A molecular dynamics study. *Chin. J. Chem.* **2012**, *30*, 1399–1404.

46. Neek-Amal, M.; Peeters, F.M. Nanoindentation of a circular sheet of bilayer graphene. *Phys. Rev. B* **2010**, *81*, doi:10.1103/PhysRevB.81.235421.

47. Reddy, C.D.; Rajendran, S.; Liew, K.M. Equilibrium configuration and continuum elastic properties of finite sized graphene. *Nanotechnology* **2006**, *17*, doi:10.1088/0957-4484/17/3/042.

48. Huang, Y.; Wu, J.; Hwang, K.C. Thickness of graphene and single-wall carbon nanotubes. *Phys. Rev. B.* **2006**, *74*, doi:10.1103/PhysRevB.74.245413.

49. Plimpton, S. Fast parallel algorithms for short-range molecular-dynamics. *J. Comput. Phys.* **1995**, *117*, 1–19.

50. Cao, G.X.; Chen, X. Buckling of single-walled carbon nanotubes upon bending: Molecular dynamics simulations and finite element method. *Phys. Rev. B* **2006**, *73*, doi:10.1103/PhysRevB.73.155435.

51. Cao, G.X.; Chen, X. The effects of chirality and boundary conditions on the mechanical properties of single-walled carbon nanotubes. *Int. J. Solids Struct.* **2007**, *44*, 5447–5465.

52. Cao, G.X.; Chen, X.; Kysar, J.W. Strain sensing of carbon nanotubes: Numerical analysis of the vibrational frequency of deformed single-wall carbon nanotubes. *Phys. Rev. B* **2005**, *72*, doi:10.1103/PhysRevB.72.195412.

53. Chen, X.; Cao, G.X. A structural mechanics study of single-walled carbon nanotubes generalized from atomistic simulation. *Nanotechnology* **2006**, *17*, doi:10.1088/0957-4484/17/4/027.

54. Shen, X.; Lin, X.Y.; Yousefi, N.; Jia, J.J.; Kim, J.K. Wrinkling in graphene sheets and graphene oxide papers. *Carbon* **2014**, *66*, 84–92.

55. Pei, Q.X.; Zhang, Y.W.; Shenoy, V.B. Mechanical properties of methyl functionalized graphene: A molecular dynamics study. *Nanotechnology* **2010**, *21*, doi:10.1088/0957-4484/21/11/115709.

56. Arroyo, M.; Belytschko, T. Finite crystal elasticity of carbon nanotubes based on the exponential cauchy-born rule. *Phys. Rev. B.* **2004**, *69*, doi:10.1103/PhysRevB.69.115415.

57. Michel, K.H.; Verberck, B. Theory of the elastic constants of graphite and graphene. *Phys. Status. Solidi B* **2008**, *245*, 2177–2180.

58. Jiang, J.W.; Wang, J.S.; Li, B.W. Young's modulus of graphene: A molecular dynamics study. *Phys. Rev. B.* **2009**, *80*, doi:10.1103/PhysRevB.80.113405.

59. Sanchez-Portal, D.; Artacho, E.; Soler, J.M.; Rubio, A.; Ordejon, P. *Ab initio* structural, elastic, and vibrational properties of carbon nanotubes. *Phys. Rev. B* **1999**, *59*, 12678–12688.

60. Hernandez, E.; Goze, C.; Bernier, P.; Rubio, A. Elastic properties of C and bxcynz composite nanotubes. *Phys. Rev. Lett.* **1998**, *80*, 4502–4505.

61. Gupta, S.; Dharamvir, K.; Jindal, V.K. Elastic moduli of single-walled carbon nanotubes and their ropes. *Phys. Rev. B* **2005**, *72*, doi:10.1103/PhysRevB.72.165428.

62. Bao, W.X.; Zhu, C.C.; Cui, W.Z. Simulation of young's modulus of single-walled carbon nanotubes by molecular dynamics. *Phys. B Condens. Matter.* **2004**, *352*, 156–163.

63. Meo, M.; Rossi, M. Prediction of young's modulus of single wall carbon nanotubes by molecular-mechanics based finite element modelling. *Compos. Sci. Technol.* **2006**, *66*, 1597–1605.

64. Chang, T.C.; Gao, H.J. Size-dependent elastic properties of a single-walled carbon nanotube via a molecular mechanics model. *J. Mech. Phys. Solids* **2003**, *51*, 1059–1074.

65. Hajgato, B.; Guryel, S.; Dauphin, Y.; Blairon, J.M.; Miltner, H.E.; van Lier, G.; de Proft, F.; Geerlings, P. Theoretical investigation of the intrinsic mechanical properties of single- and double-layer graphene. *J. Phys. Chem. C* **2012**, *116*, 22608–22618.

66. Hemmasizadeh, A.; Mahzoon, M.; Hadi, E.; Khandan, R. A method for developing the equivalent continuum model of a single layer graphene sheet. *Thin Solid Films* **2008**, *516*, 7636–7640.

67. Terdalkar, S.S.; Huang, S.; Yuan, H.Y.; Rencis, J.J.; Zhu, T.; Zhang, S.L. Nanoscale fracture in graphene. *Chem. Phys. Lett.* **2010**, *494*, 218–222.

68. Shen, Y.K.; Wu, H.A. Interlayer shear effect on multilayer graphene subjected to bending. *Appl. Phys. Lett.* **2012**, *100*, doi:10.1063/1.3693390.

69. Jing, N.N.; Xue, Q.Z.; Ling, C.C.; Shan, M.X.; Zhang, T.; Zhou, X.Y.; Jiao, Z.Y. Effect of defects on young's modulus of graphene sheets: A molecular dynamics simulation. *RSC Adv.* **2012**, *2*, 9124–9129.

70. Neek-Amal, M.; Peeters, F.M. Linear reduction of stiffness and vibration frequencies in defected circular monolayer graphene. *Phys. Rev. B* **2010**, *81*, doi:10.1103/PhysRevB.81.235437.

71. Wei, X.D.; Kysar, J.W. Experimental validation of multiscale modeling of indentation of suspended circular graphene membranes. *Int. J. Solids Struct.* **2012**, *49*, 3201–3209.

72. Cao, G. Graphene: An anisotropic two-dimensional tensegrity. *Carbon* **2014**, unpublished.

73. Bunch, J.S.; Verbridge, S.S.; Alden, J.S.; van der Zande, A.M.; Parpia, J.M.; Craighead, H.G.; McEuen, P.L. Impermeable atomic membranes from graphene sheets. *Nano Lett.* **2008**, *8*, 2458–2462.

74. Han, J.; Ryu, S.; Sohn, D.; Im, S. Mechanical strength characteristics of asymmetric tilt grain boundaries in graphene. *Carbon* **2014**, *68*, 250–257.

75. Jhon, Y.I.; Zhu, S.E.; Ahn, J.H.; Jhon, M.S. The mechanical responses of tilted and non-tilted grain boundaries in graphene. *Carbon* **2012**, *50*, 3708–3716.

76. Ovid'ko, I.A.; Sheinerman, A.G. Cracks at disclinated grain boundaries in graphene. *J. Phys. D Appl. Phys.* **2013**, *46*, doi:10.1088/0022-3727/46/34/345305.

77. Jhon, Y.I.; Chung, P.S.; Smith, R.; Min, K.S.; Yeom, G.Y.; Jhon, M.S. Grain boundaries orientation effects on tensile mechanics of polycrystalline graphene. *RSC Adv.* **2013**, *3*, 9897–9903.

78. Liu, T.H.; Gajewski, G.; Pao, C.W.; Chang, C.C. Structure, energy, and structural transformations of graphene grain boundaries from atomistic simulations. *Carbon* **2011**, *49*, 2306–2317.

79. Yi, L.J.; Yin, Z.N.; Zhang, Y.Y.; Chang, T.C. A theoretical evaluation of the temperature and strain-rate dependent fracture strength of tilt grain boundaries in graphene. *Carbon* **2013**, *51*, 373–380.

80. Wei, Y.J.; Wu, J.T.; Yin, H.Q.; Shi, X.H.; Yang, R.G.; Dresselhaus, M. The nature of strength enhancement and weakening by pentagon-heptagon defects in graphene. *Nat. Mater.* **2012**, *11*, 759–763.

81. He, L.C.; Guo, S.S.; Lei, J.C.; Sha, Z.D.; Liu, Z.S. The effect of stone-thrower-wales defects on mechanical properties of graphene sheets—A molecular dynamics study. *Carbon* **2014**, *75*, 124–132.

82. Yazyev, O.V.; Louie, S.G. Topological defects in graphene: Dislocations and grain boundaries. *Phys. Rev. B* **2010**, *81*, doi:10.1103/PhysRevB.81.195420.

83. Lee, G.H.; Cooper, R.C.; An, S.J.; Lee, S.; van der Zande, A.; Petrone, N.; Hammerherg, A.G.; Lee, C.; Crawford, B.; Oliver, W.; *et al.* High-strength chemical-vapor deposited graphene and grain boundaries. *Science* **2013**, *340*, 1073–1076.

84. Zhang, J.F.; Zhao, J.J.; Lu, J.P. Intrinsic strength and failure behaviors of graphene grain boundaries. *ACS Nano* **2012**, *6*, 2704–2711.